Supplemental Information

Hierarchically Encapsulated Phase-Change Film with Multi-stage Heat Management Properties and Conformable Self-Interfacing Contacts for Enhanced Interface Heat Dissipation

Qing Lu[1#], Xiang Wang[2#*], Hong-wei Zhao[3], Xun-rui Wang[1], Jia-qing Zhao[1], Hao-ran Kong[2], Tao Wang[1], Chao Liang[1], Jin-hong Li[1*], Wayne Qiang Xu[4*]

[1] *Beijing Key Laboratory of Materials Utilization of Nonmetallic Minerals and Solid Wastes, National Laboratory of Mineral Materials, School of Materials Science and Technology, China University of Geosciences, Beijing 100083, P. R. China.*

[2] *State Key Laboratory of Multiphase Complex Systems, Institute of Process Engineering, Chinese Academy of Sciences, Beijing, 100190, P. R. China*

[3] *Key Laboratory of Cryogenics, Technical Institute of Physics and Chemistry, Chinese Academy of Science, Beijing, 100190, P. R. China*

[4] *Forward Industrial Research Institute, Shenzhen, 518000, P. R. China*

***Corresponding authors, Email address:** *wangxiang@ipe.ac.cn; jinhong@cugb.edu.cn; xwq@qianzhan.com*

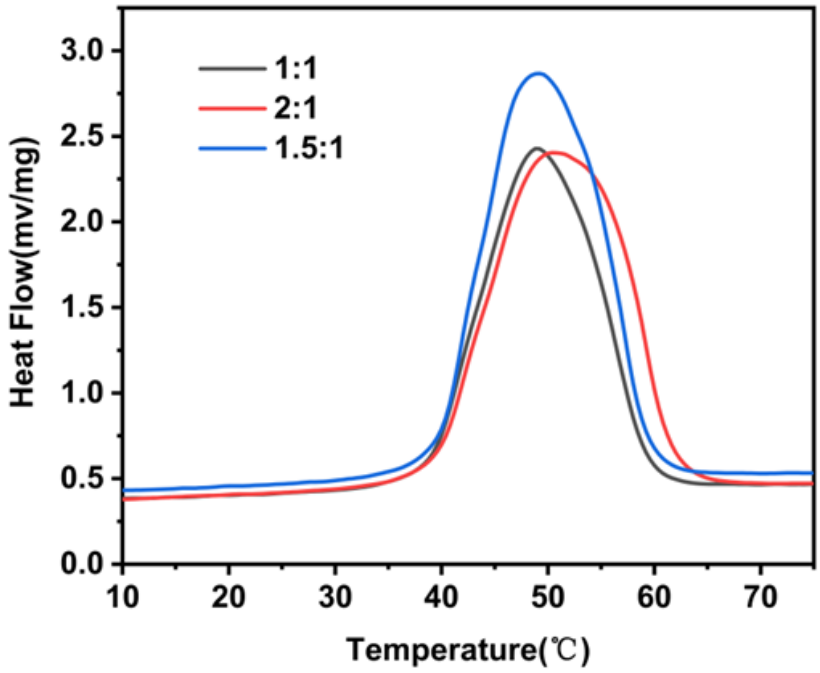

Figure S1. DSC curves of microcapsules with different core/shell material ratios.

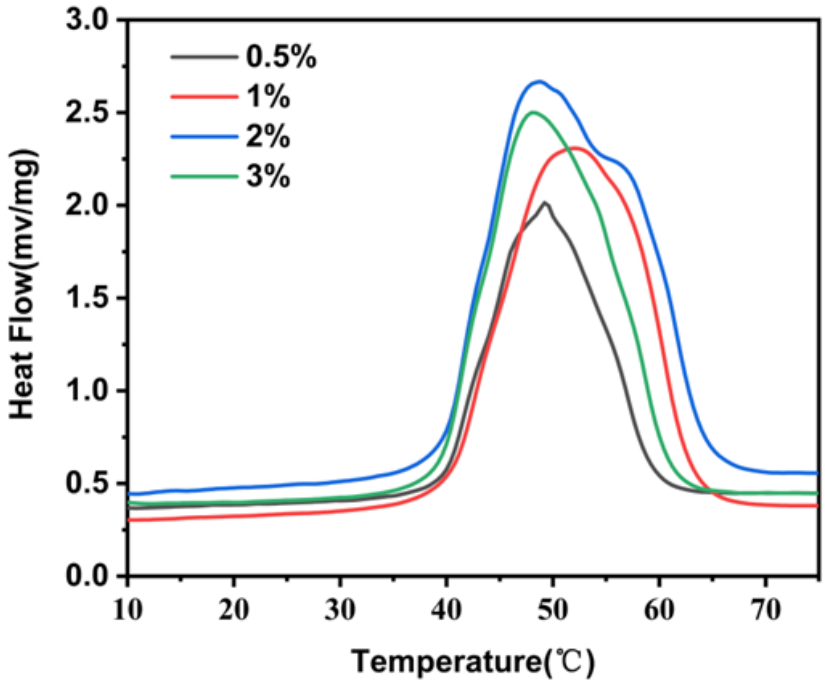

Figure S2. DSC curves of microcapsules with different initiator concentrations.

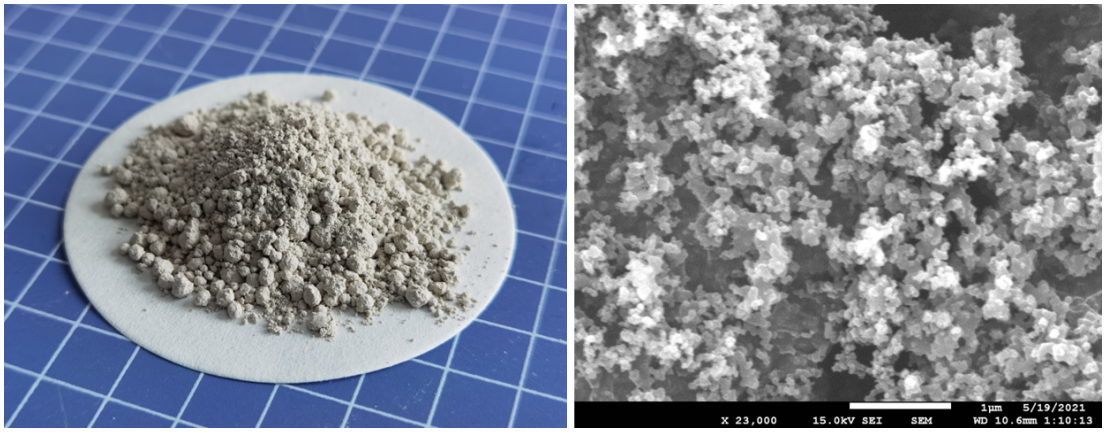

Figure S3. Digital photo and SEM image of *n*-Si_3N_4 powder.

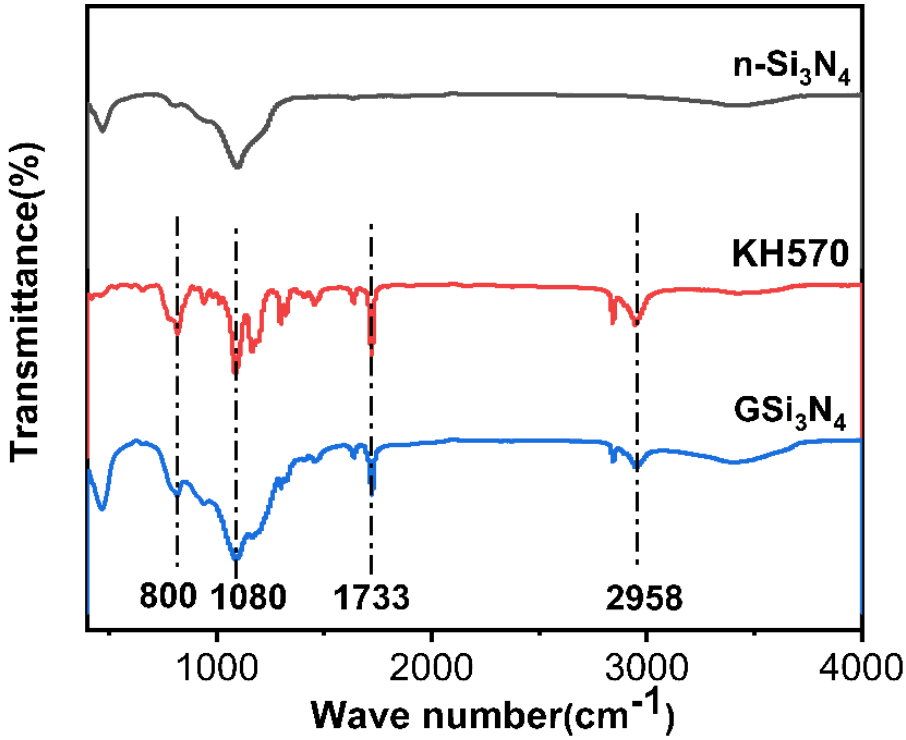

Figure S4. FT-IR spectrum of Si_3N_4 particles before and after KH570 treatment

The new peaks in the infrared spectrum of the modified Si_3N_4 (G-Si_3N_4) appeared at 2958 cm^{-1}, 1733 cm^{-1}, 800 cm^{-1} and 1080 cm^{-1}, which are corresponding to the -CH_3 stretching vibration absorption peak, the absorption peak of C=O in ester, and the silicon oxy silicon bond, conforming that KH-570 silane coupling agent has been successfully grafted onto the surface of Si_3N_4 particles.

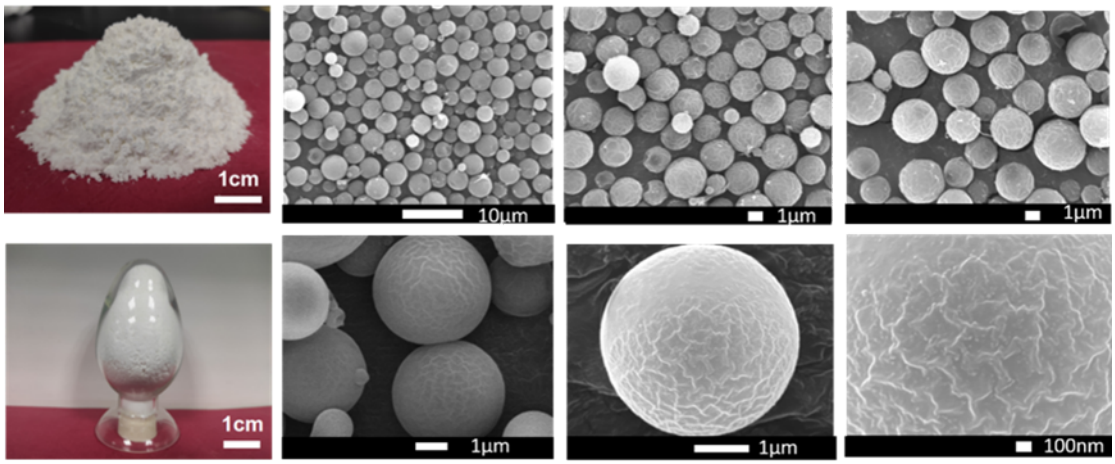

Figure S5. Optical photographs and SEM images of phase change microcapsules (GMPCM2.5) with different proportions of *n*-Si_3N_4 additions.

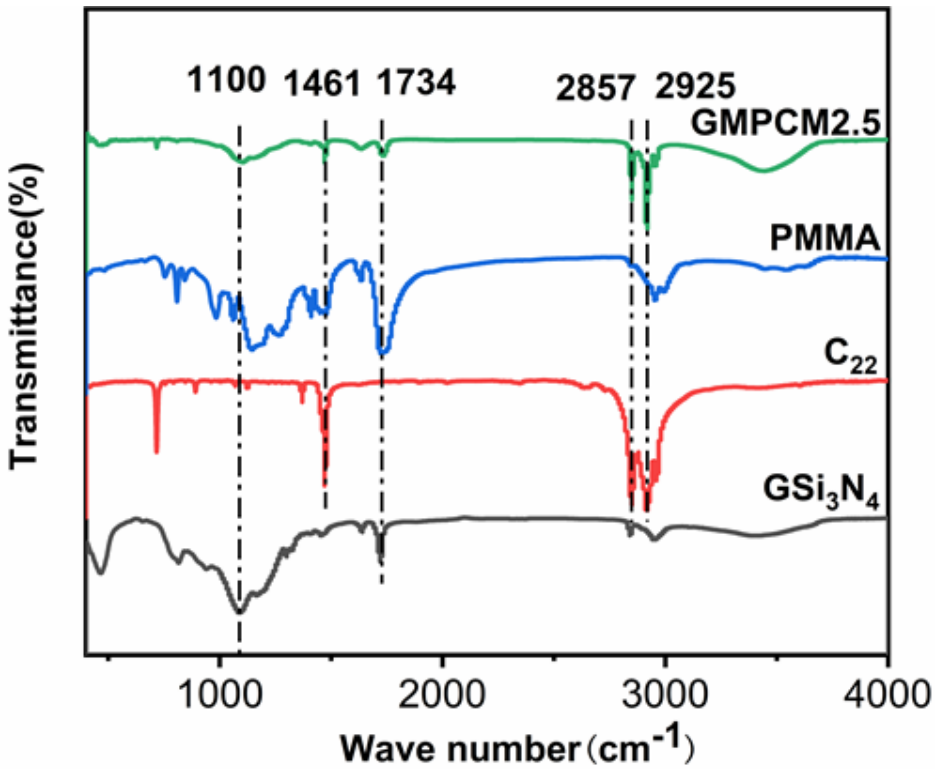

Figure S6. FT-IR spectra of GMPCM2.5, PMMA, C_{22}, and G-Si_3N_4.

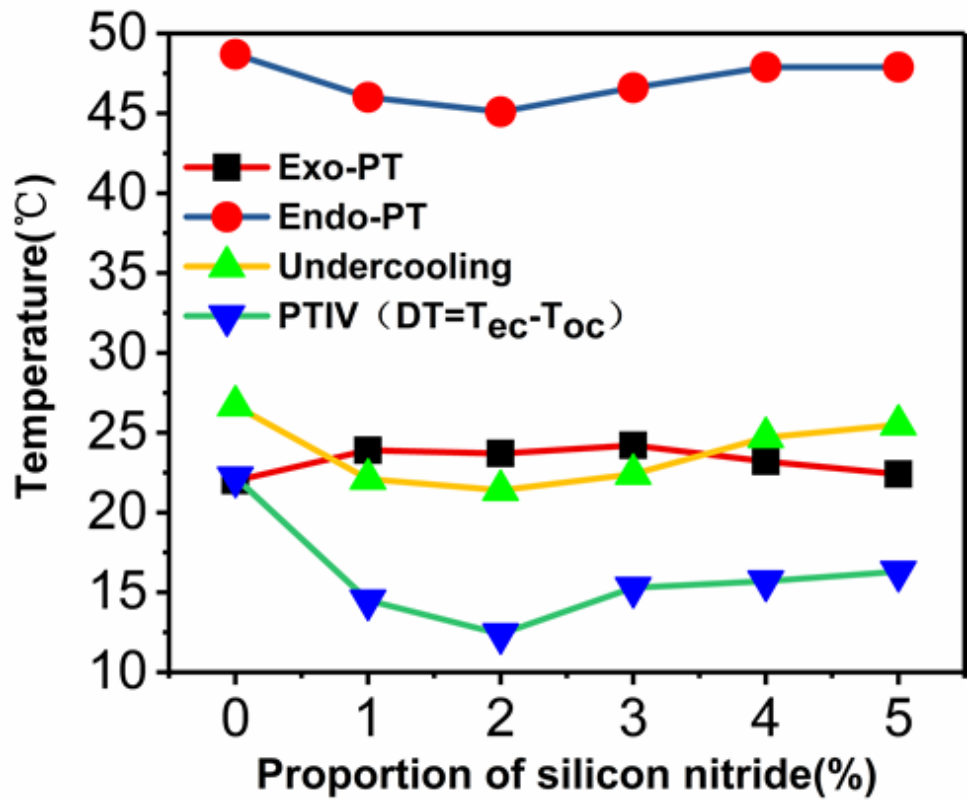

Figure S7. Influences of proportion of silicon nitride on the degree of subcooling of n-docosane.

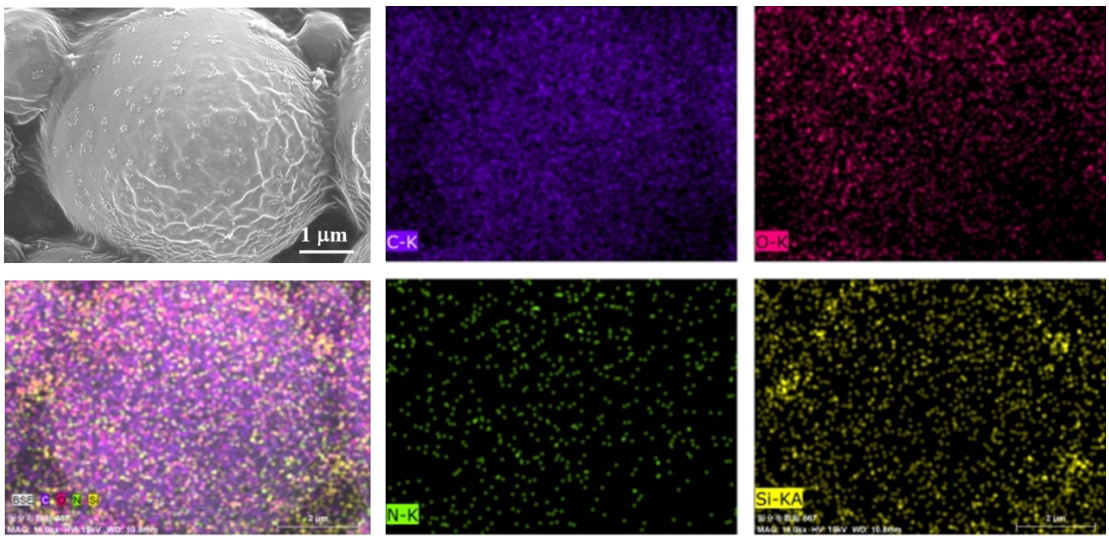

Fig. S8 SEM images and related elemental mapping analysis of *n*-Si_3N_4 hybrid PCM microcapsules.

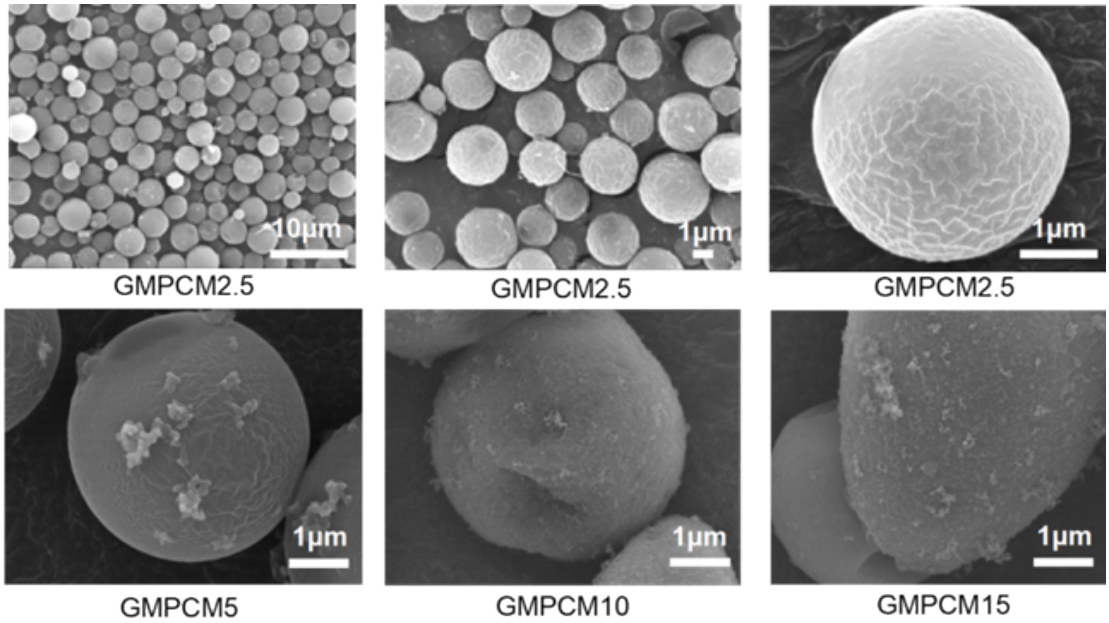

Fig. S9 SEM images of n-Si_3N_4 hybrid PCM microcapsules with different n-Si_3N_4 proportions.

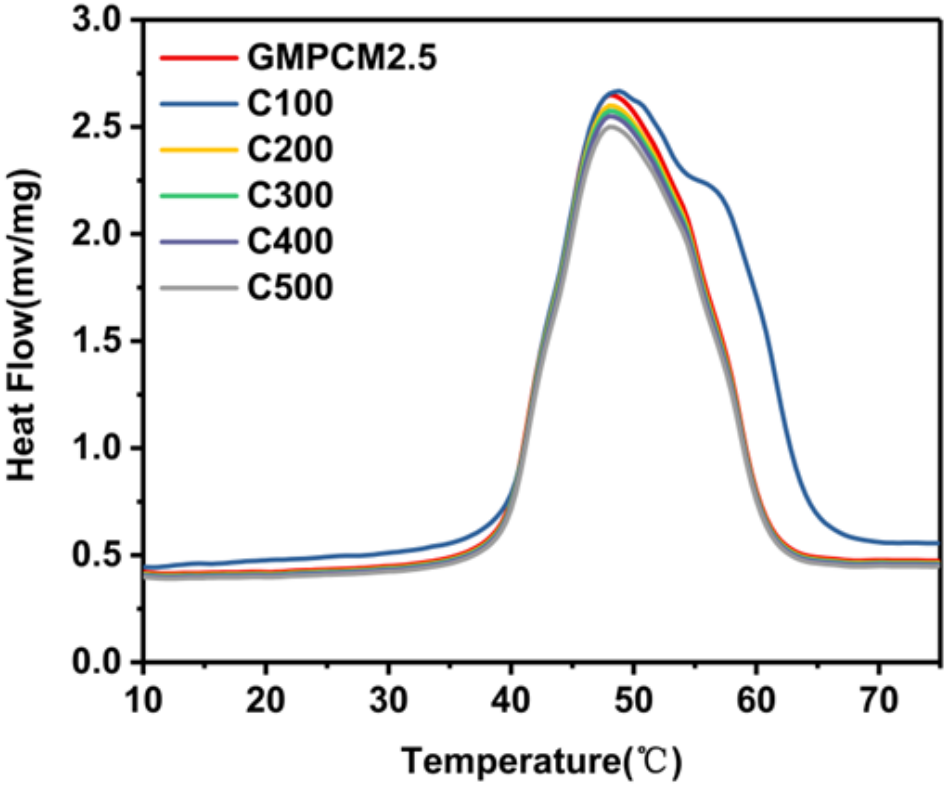

Figure S10. DSC curves of GMPCM2.5 after different heating and cooling cycles.

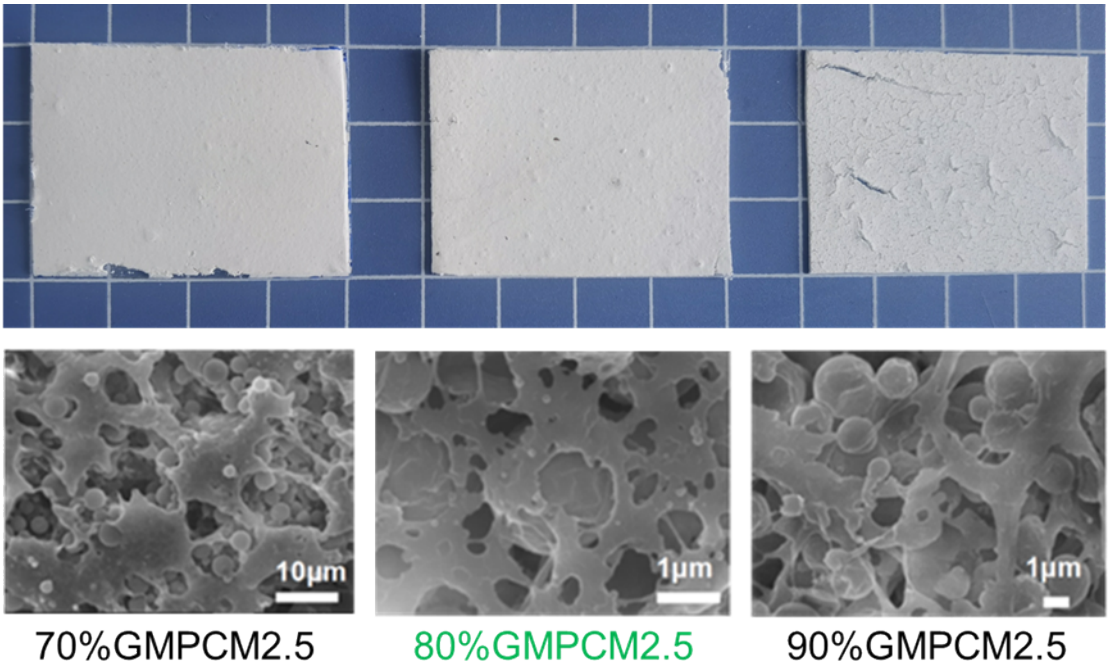

Figure S11. The digital photos and SEM images of the porous phase change film with different GMPCM2.5 proportions.

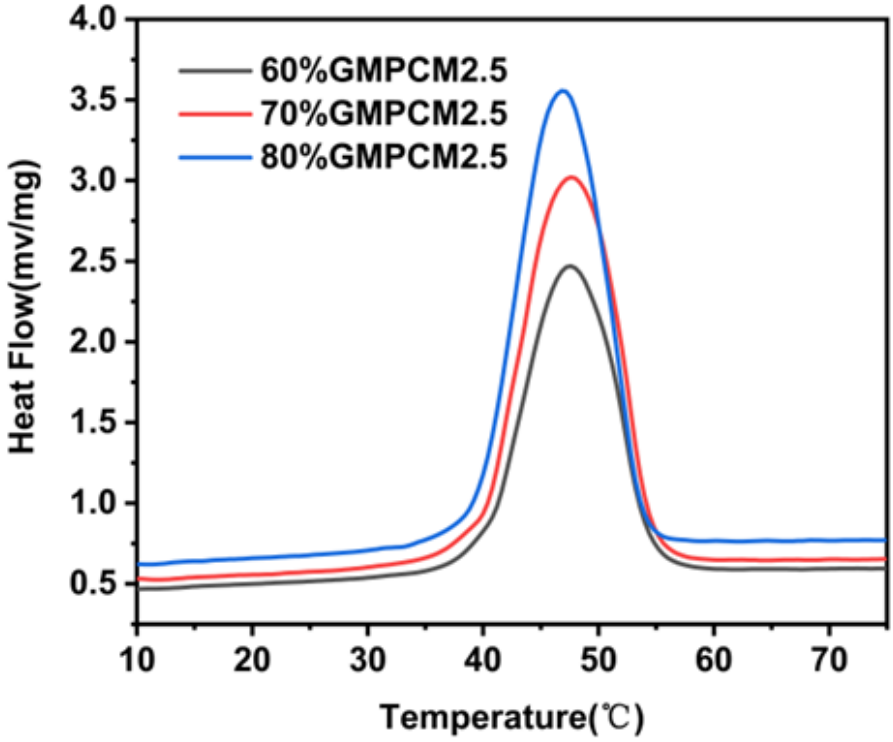

Figure S12. DSC curves of porous phase-change microcapsule films with different volume proportions of GMPCM2.5.

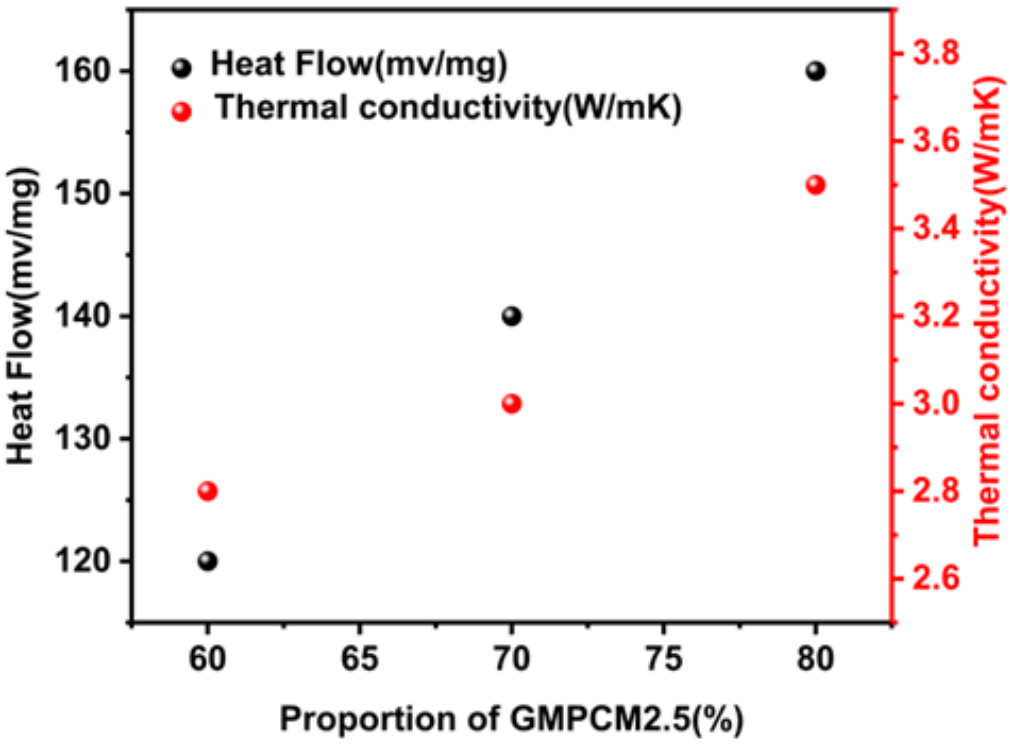

Figure S13. Thermal storage (heat flow) and thermal conductivity of porous phase-change microcapsule films with different volume proportions of GMPCM2.5.

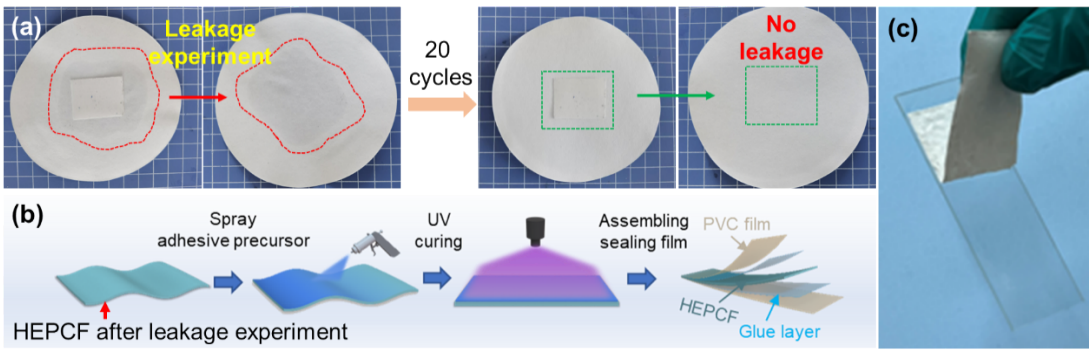

Figure S14 (a) Leakage experiments, (b) surface sealing procedures and (c) interfacial bonding performance of HEPCF.

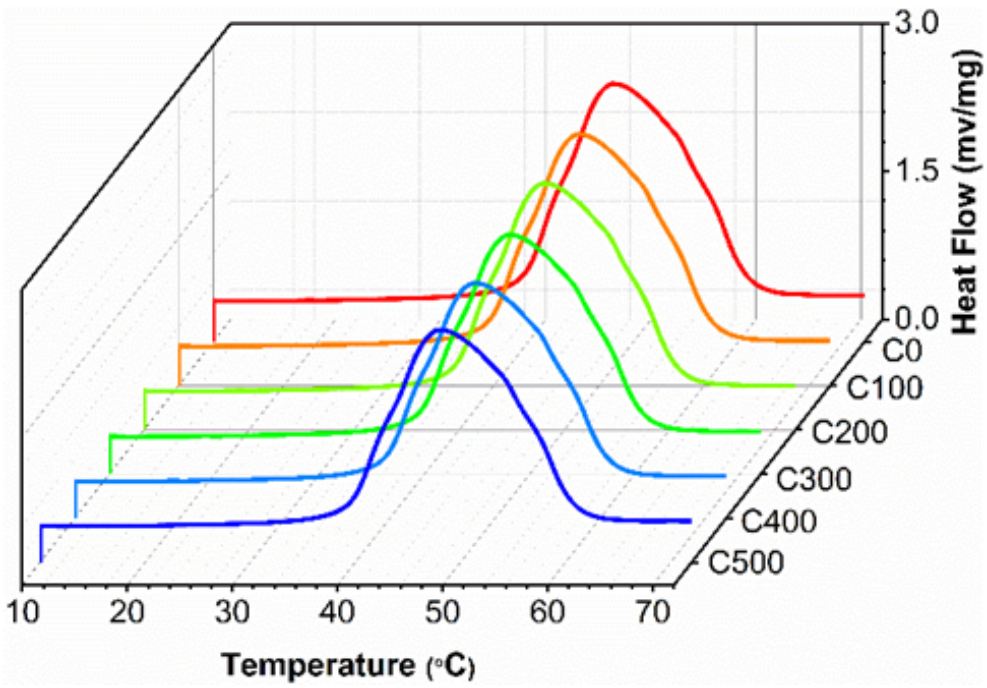

Figure S15. DSC curves of HEPCF with 80% volume proportions of GMPCM2.5 after different heating and cooling cycles.

The contribution of heat conduction and energy absorption of the developed phase change thermal interface material sample has been quantified by the Transient-Hot-Wire (THW) method (Fig.S15a) at its theoretical phase change temperature under a constant thermal diffusion flux of 1.0×10^{-5} m^2/s, where a normal non-phase change sample with same thermal conductivity was used as control sample. All samples were kept at 25 °C before the test. Then, two pieces of each tested samples (3 cm × 4 cm) were attached tightly to the THW test chip (XIATech® TC-3100) placed in an incubator at 45 °C (theoretical phase change temperature of HEPCF), and the real-time thermal conductivity data *vs* holding time (κ vs t) was also recorded until the thermal conductivity values of the two samples themselves converged, shown as Fig S15b. According to the definition of thermal conductivity (κ), it is determined by the thermal diffusivity (α), density (ρ) and specific heat capacity (C_p) of the material, shown as follows in equation (S1):

$$\kappa = \alpha\rho c_p \qquad \text{(S1)}$$

The thermal diffusion flux (α) was kept constant at 1.0×10^{-5} m^2/s, and the density (ρ) of the two samples were similar with 0.75 g/ cm^3. Thus, the thermal conductivity of the tested sample is proportional to its specific heat capacity. The instantaneous thermal conductivity increase of the HEPCF sample during its isothermal phase change process could be considered as its additional energy absorption contribution part. Therefore, the whole contribution of heat conduction and energy absorption of the HEPCF sample during its phase change process can be calculated by integration of the area under the κ vs t curves of the HEPCF and control sample, respectively. By calculation, the heat conduction and energy absorption of the HEPCF sample accounts for 68.6% and 31.4%, respectively, which can effectively absorb the instantaneous local heat.

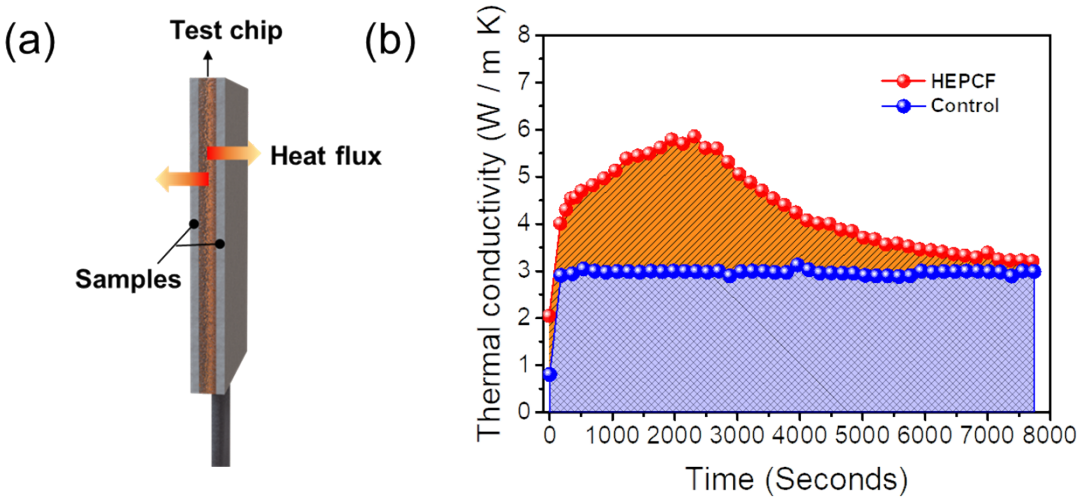

Figure S16. (a) Schematic diagram of the Transient-Hot-Wire (THW) test method and (b) the real-time thermal conductivity *vs* holding time (κ vs t) curves at constant ambient temperature of 45 °C.

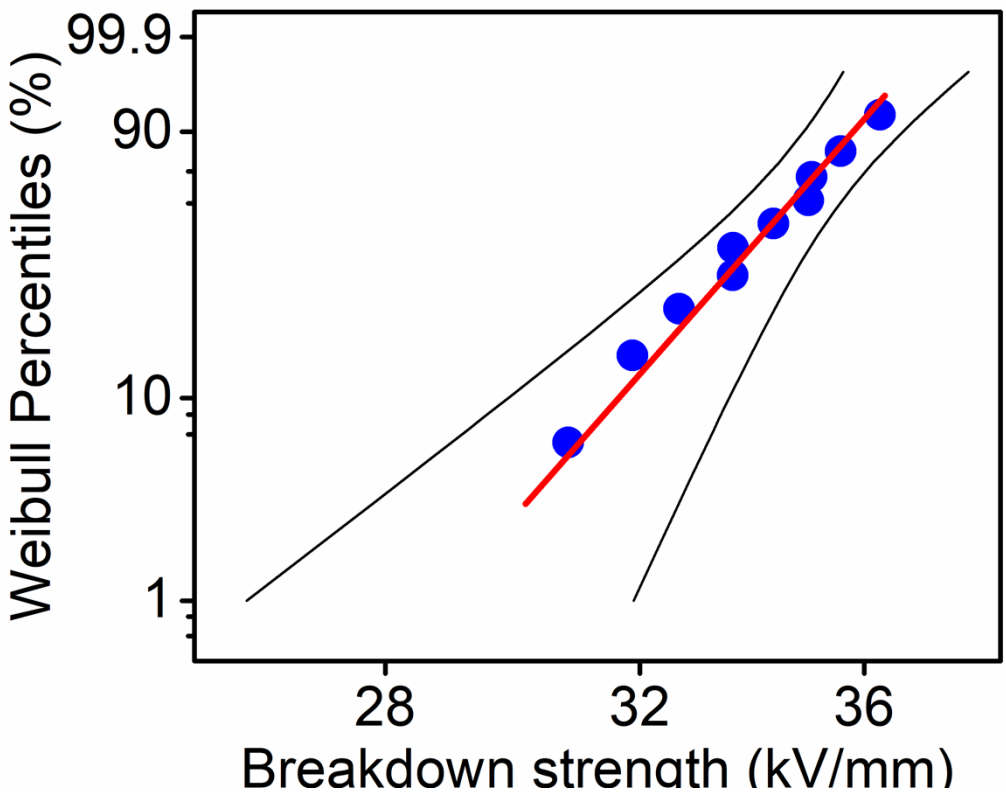

Figure S17. Weibull probability plot of the breakdown voltage of HEPCF.

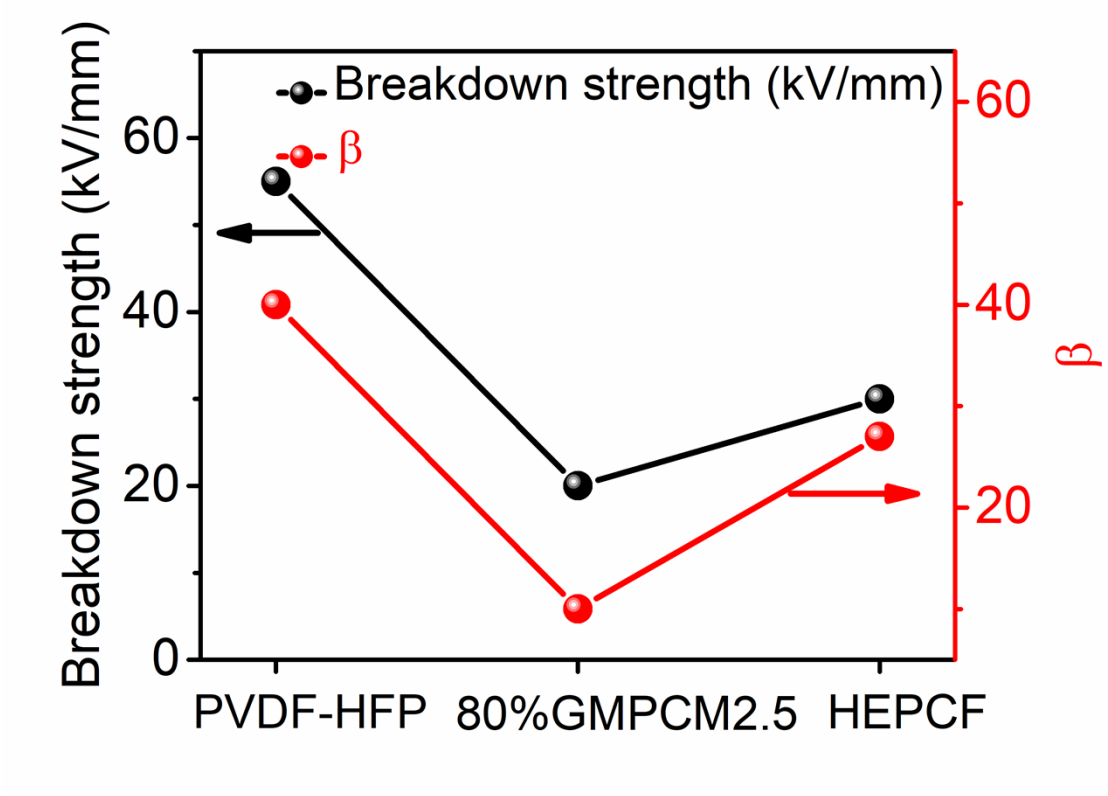

Figure S18. Breakdown field strength of the PhC-TIM films with different PCM. loadings

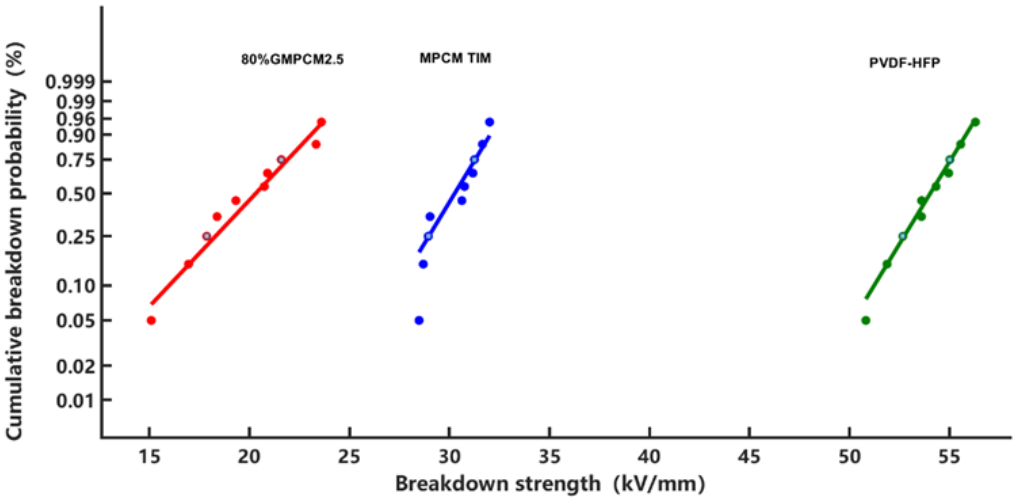

Figure S19. Weibull probability plots of the breakdown voltage with different MPCM loadings.

The contribution of heat conduction and energy absorption in the HEPCF has been quantified by the Transient-Hot-Wire (THW) method at its theoretical phase change temperature under a constant thermal diffusion, where a normal non-phase change sample with same thermal conductivity was used as control sample. The thermal contact resistances between the copper plates and HEPCF sample were calculated by using the following equations (S2)-(S5):

$$R = R_{Cu} + R_i \quad \text{(S2)}$$

$$R_i = R_{bulk} + R_c = BLT/\kappa_{eff} \quad \text{(S3)}$$

$$R_{bulk} = BLT/\kappa_{HEPCF} \quad \text{(S4)}$$

$$R_c = R_{c1} + R_{C2} \quad \text{(S5)}$$

where R is the total thermal resistance of the sandwiched thermal interface, R_{Cu} is the thermal resistance of copper plates at the hot side and cold side, R_i is the total resistance of the interface between two copper plates, R_{bulk} is the intrinsic thermal resistance of the HEPCF, R_c is the thermal contact resistance between the HEPCF and the double sides, BLT is the bond line thickness, κ_{eff} is the effective thermal conductivity of the HEPCF, κ_{HEPCF} is the intrinsic thermal conductivity of the HEPCF. BLT was obtained by subtracting the thickness of two copper plates from the total thickness of sandwiched thermal interface. The BLT of HEPCF used for thermal property measurements were about 425 μm.

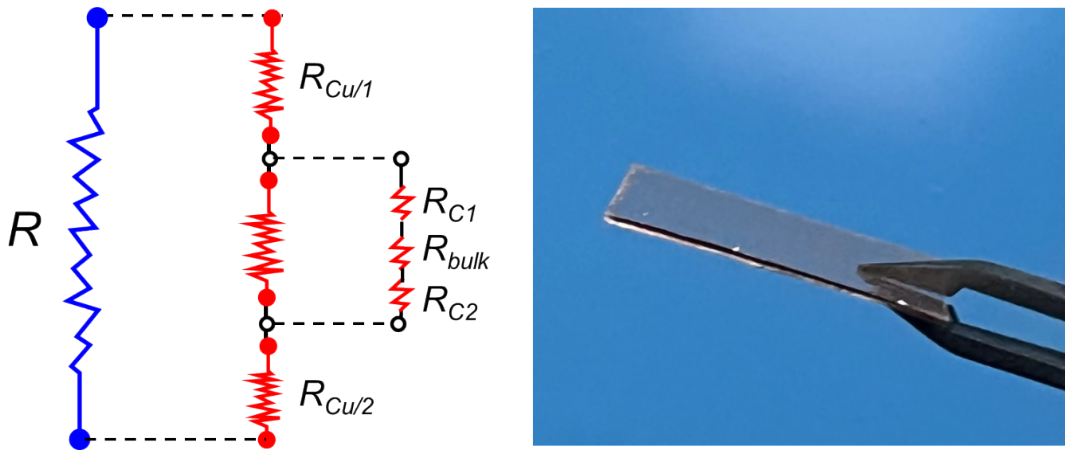

Figure S20. Schematic diagram of thermal resistance in series and the digital photograph of the sandwiched sample.

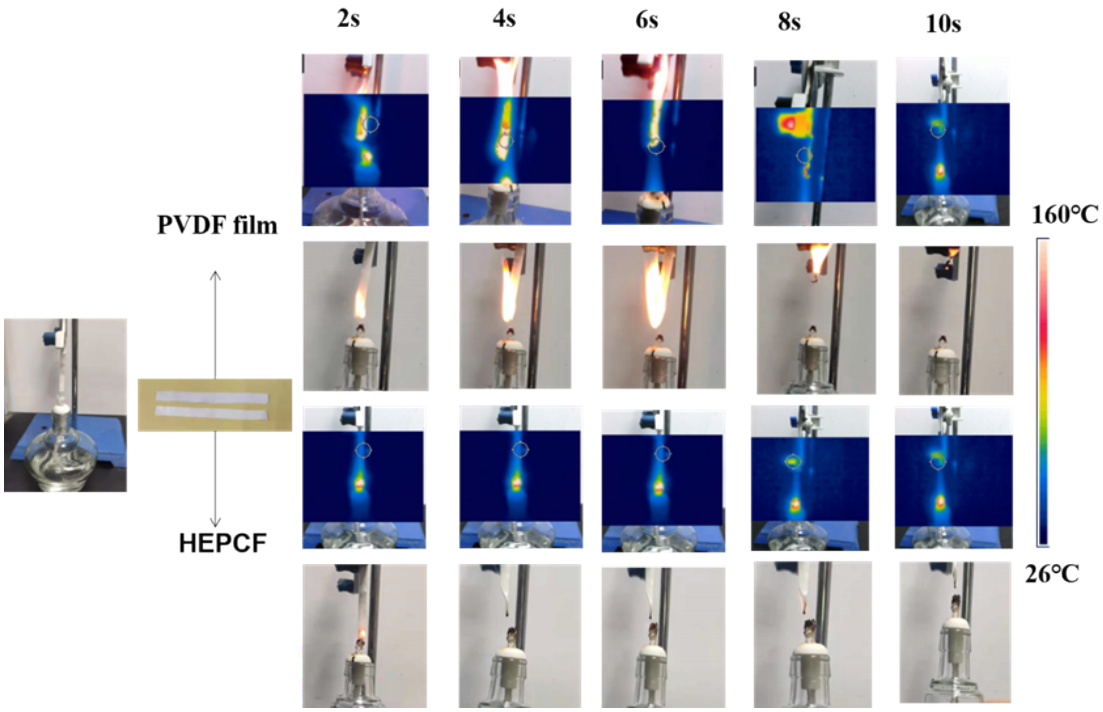

Figure S21. Flame retardant properties of PVDF-HFP and HEPCF samples.

The surface temperature of the simulated thermal runaway battery can reach up to 160 ºC in 30 seconds by adjusting the voltage and current, which has reached the initial explosion temperature of the lithium-ion battery, and the thermal failure [1] state of the battery is successfully simulated.

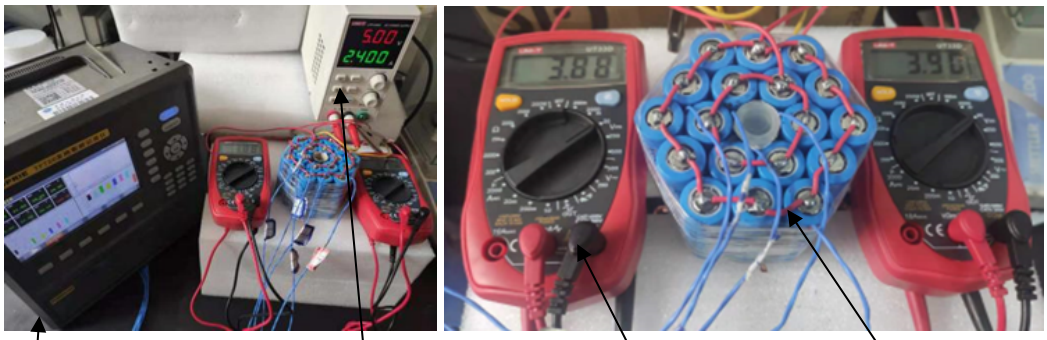

Multiplex temp. recorder **DC power supply** **Multimeter** **Simulated battery model**

Figure S22. Physical illustration of thermal runway battery simulation unit.

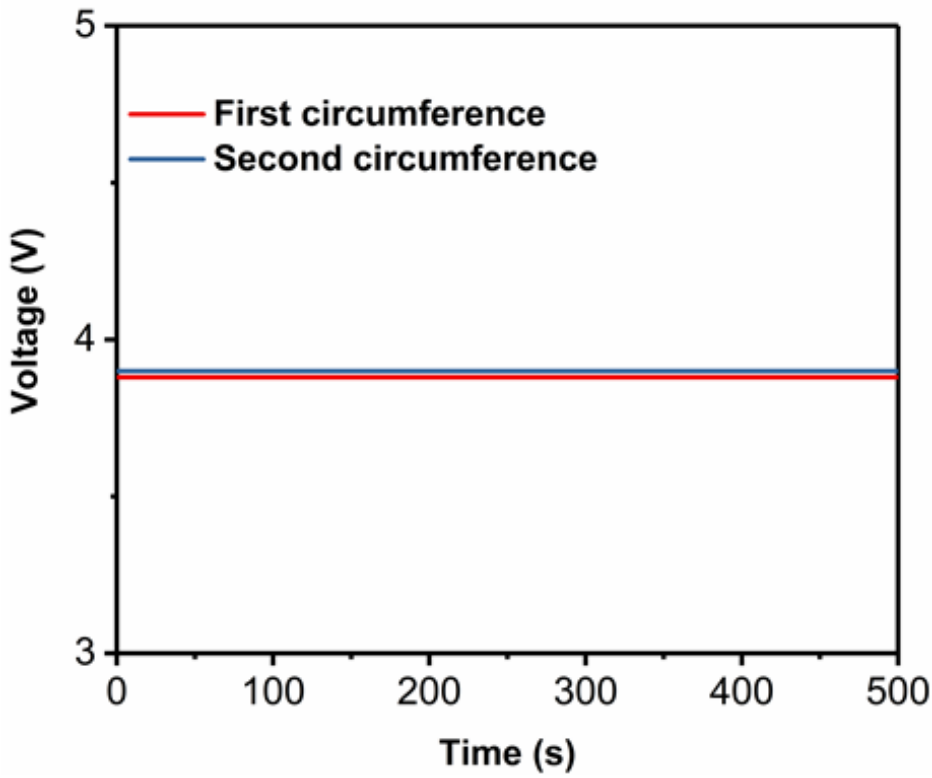

Figure S23. Effect of the simulated thermal failure cell equipped with HEPCF on the voltages of the surrounding battery cells.

The thermal management performance of the developed HEPCF phase change thermal interface material was tested by comparing the temperature profiles of a commercial 18650 lithium-ion battery unit with and without equipment the HEPCF film during the multiple charging and discharging cycles. The schematic diagram of the tested battery pack is shown as Fig. S23a.The two circles of the outer-side batteries were placed in parallel and shoulder to shoulder to the target battery and every red dot labeled on the given battery represents a monitoring thermocouple. The outer-side battery module was connected to a 10W graphite belt resistor to simulate the normal working state of the battery. At the same time, the target battery unit in the center was charged and discharged under different currents by a DC source monitored by a DC ammeter (0-10A). The results demonstrated that the maximum surface temperatures (spot 1) reached 55.2 ºC and 88.9 ºC (thermal failure occurred) for the battery unit with (Fig. S23b) and without (Fig. S23c) wrapping the HEPCF film after continuous charge and discharge testing. Especially, the thermal runaway of the HEPCF protect battery unite was effectively inhibited, which guarantee the battery safety.

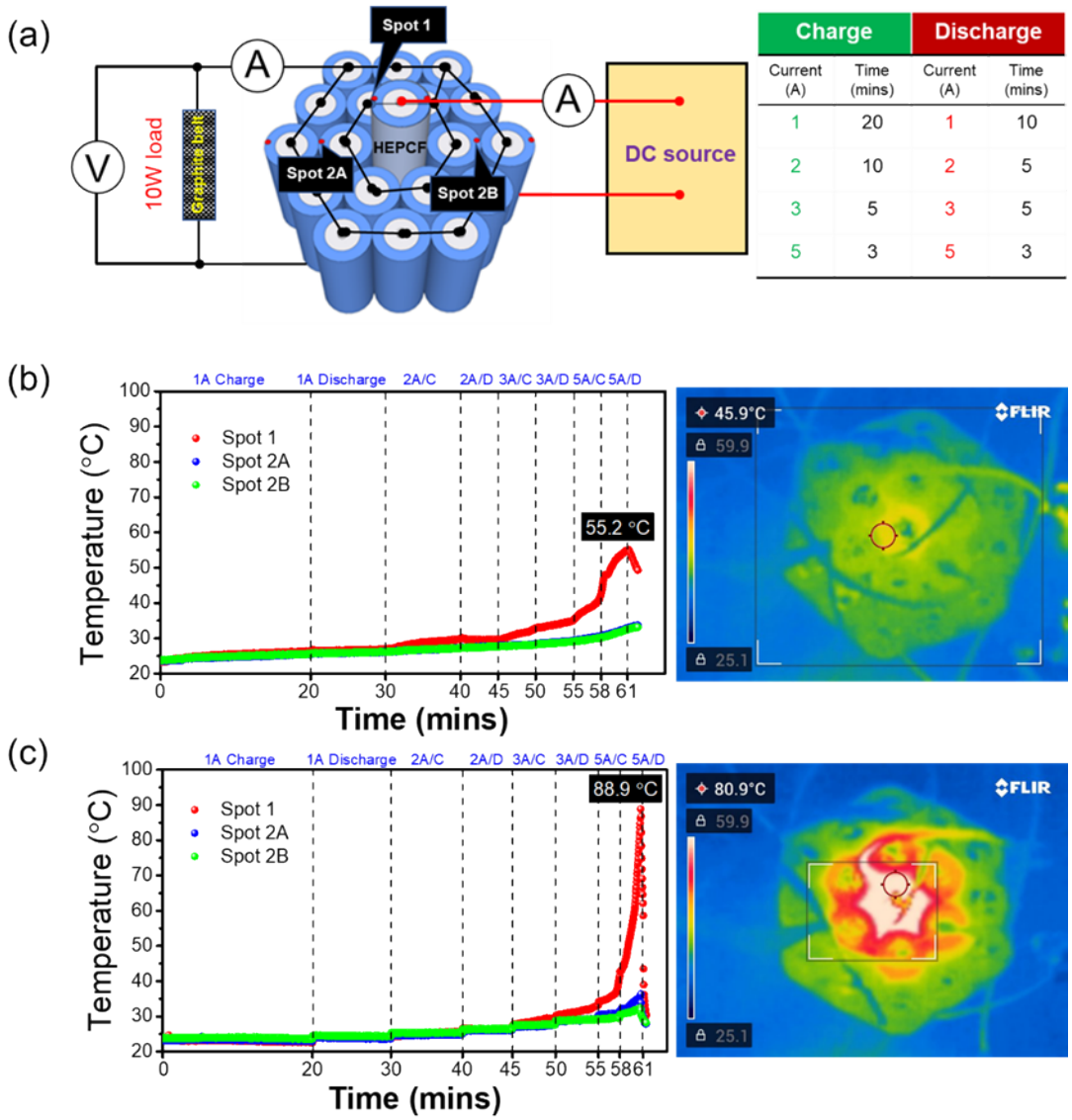

Fig. S24. (a) Schematic diagram and parameters of the charging-discharging test Li-ion battery pack, temperature profiles of the monitored hot-spot temperatures of the Li-ion battery pack (b) with and (c) without wrapping of HEPCF during multiple charging and discharging cycles.

Table S1. Factors and levels of L_9 (4^3) orthogonal experiments

Levels	Factors			
	A Initiator content (wt%)	B Core/shell ratio	C Stirring speed (rpm)	D Reaction temperature (ºC)
1	1%	0.5:1	300	65
2	3%	1.5:1	600	75
3	5%	2.5:1	900	85

Table S2. Results for encapsulation rates under orthogonal experiments

Groups	A	B	C	D	Encapsulation rate (%)
1	1	1	1	1	60.0
2	1	2	2	2	77.5
3	1	3	3	3	71.5
4	2	1	2	3	34.2
5	2	2	3	1	64.1
6	2	3	1	2	51.8
7	3	1	3	2	41.2
8	3	2	1	3	66.8
9	3	3	2	1	74.4
K1	69.7	45.1	59.5	66.2	
K2	50.0	69.4	62.0	56.8	
K3	60.8	65.9	58.9	57.5	
Excellent level	A1	B2	C3	D1	
Range R	19.7	24.3	3.1	9.4	
Primary and secondary order	B	A	D	C	

By designing L9 (4^3) orthogonal experiments [2], the preparation conditions of phase change microcapsules with optimized encapsulation rate were obtained. By discussing the influencing factors such as initiator, reaction temperature, core-shell ratio, stirring speed for the encapsulation rate of the microcapsules [3], the optimized conditions were obtained. From the above experiments, it can be concluded that the core/shell ratio has the greatest influence on the encapsulation rate of the microcapsules, followed by the initiator content, and finally the reaction temperature and stirring speed. The results showed that the optimal reaction conditions for the preparation of phase change microcapsule are A1B2C3D1. Since the core/shell material ratio and initiator content are very important, thus the influence of these two factors on the encapsulation rate of microcapsules was further studied.

Table S3. The effect of core/shell material ratio on the encapsulation rate of microcapsules

Groups	Core/shell ratio	Encapsulation rate（%）
1	1:1	60.8
2	1.5:1	73.7
3	2:1	71.0
4	2.5:1	\

Table S4. The influence of core/shell material ratios on the melting temperature (TM) and the melting enthalpy (HM) of the prepared microcapsules

Samples	Melting process	
	T_m (ºC)	H_m (J/g)
1:1	49.0	150.7
1.5:1	50.5	182.4
2:1	49.2	175.8

Table S5. The effect of initiator concentration on the encapsulation rate of microcapsules

Samples	Initiator concentration (wt%)	Encapsulation rate（%）
1	0.5	47.0
2	1	71.5
3	2	84.7
4	3	69.7

Table S6. The influence of the initiator concentrations on the melting temperature (TM) and the melting enthalpy (HM) of the prepared microcapsules

Samples	Melting process	
	T_m (ºC)	H_m (J/g)
0.5%	49.4	116.4
1%	51.9	177.1
2%	48.8	210.0
3%	50.4	171.4

In conclusion, the optimized conditions can be obtained from the above results: the initiator concentration is 2%, the reaction temperature is 65 °C, the core/shell ratio is 1.5:1, and the stirring speed is 900 rpm. Under the above conditions, the enthalpy value of the obtained phase change microcapsules is as high as 210 J/g, and the encapsulation rate is as high as 84.7%.

Table S7. Mass density, specific heat, thermal diffusivity, and thermal conductivity of the GMPCM-X samples

GSi_3N_4 loading (wt%)	Mass density ρ (kg/m^3)	Specific heat c_p (J/kg·K)	Thermal diffusivity (m^2/s)	Thermal conductivity (W / m · K)
GMPCM-0	778	2197	0.088×10^{-6}	0.147
GMPCM-2.5	750	1720	3.719×10^{-6}	4.8
GMPCM-5	700	1562	5.212×10^{-6}	5.7
GMPCM-10	690	1222	7.175×10^{-6}	6.05
GMPCM-15	660	1112	8.437×10^{-6}	6.214

Table S8. Thermal performance of C_{22} and phase change microcapsules with different addition amount of G-Si_3N_4

Samples	Melting process		Calculated encapsulation rate（%）
	T_m (ºC)	H_m (J/g)	
C_{22}	48.7	247.9	100
GMPCM-0	48.8	210.0	84.7
GMPCM-2.5	51.8	213.7	86.2
GMPCM-5.0	51.6	202	81.4
GMPCM-10.0	48.7	192.8	77.7
GMPCM-15.0	51.9	161.9	65.3

Table S9. Thermal performance of n-docosane with different proportions (wt%) of G-Si_3N_4

Sample	ΔH_C (J/g)	T_{oc} (ºC)	T_{pc} (ºC)	T_{ec} (ºC)	ΔH_m (J/g)	T_{om} (ºC)	T_{pm} (ºC)	T_{em} (ºC)
C22-0	-265.6	31.5	22	11.1	247.9	38.7	48.7	60.9
C22-1	-197.7	31.1	23.9	17.1	240.5	38.5	46	53
C22-2	-245.4	28.8	23.7	17.5	250.1	38.9	47.8	51.3
C22-3	-251.3	32.7	24.2	16.8	237.2	39.5	46.6	54.8
C22-4	-241.9	32.5	23.2	16.5	233.7	39.6	47.9	55.3
C22-5	-241.8	32.2	22.4	15.1	229.5	39.8	47.9	56.1

Table S10 Mass density, specific heat, thermal diffusivity, and thermal conductivity of GMPCM2.5 after different heating and cooling cycles

Cycle numbers	Mass density (ρ, kg / m^3)	Specific heat (C_p, J / kg · K)	Thermal diffusivity α (m^2 / s)	Thermal conductivity (κ, W / m · K)
0	780	1669	2.919×10^{-6}	3.8
100	780	1708	2.701×10^{-6}	3.6
200	775	1909	2.500×10^{-6}	3.7
300	770	1819	2.498×10^{-6}	3.5
400	768	1890	2.479×10^{-6}	3.6
500	765	2020	2.329×10^{-6}	3.6

Table S11. Thermal performance of porous phase-change microcapsule films with different volume proportions of GMPCM2.5 loading

Samples	Melting process		Actual coverage rate（%）	film thickness(mm)
	T_m (ºC)	H_m (J/g)		
GMPCM2.5	49.1	213.7	100	\
60%GMPCM2.5	47.5	120	56.1%	0.216
70%GMPCM2.5	47.6	140	65.5%	0.186
80%GMPCM2.5	47	160	74.8%	0.154

Table S12. Mass density, specific heat, thermal diffusivity, and thermal conductivity of porous phase-change microcapsule films with different quality proportions of GMPCM2.5

GMPCM2.5 loading（wt%）	Mass density (ρ, kg / m3)	Specific heat (C_p, J / kg · K)	Thermal diffusivity α (m^2 / s)	Thermal conductivity (κ, W / m · K)
60	850	1916	1.719×10^{-6}	2.8
70	750	1599	2.501×10^{-6}	3
80	600	1881	3.100×10^{-6}	3.5

Table S13. Mass density, specific heat, thermal diffusivity, and thermal conductivity of HEPCF after different heating and cooling cycle

Cycle Times	Mass density (ρ, kg / m^3)	Specific heat (C_p, J / kg · K)	Thermal diffusivity α (m^2 / s)	Thermal conductivity (κ, W / m · K)
0	750	1720	3.719×10^{-6}	4.8
100	750	1693	3.701×10^{-6}	4.7
200	750	1729	3.700×10^{-6}	4.8
300	749	1624	3.698×10^{-6}	4.5
400	746	1676	3.679×10^{-6}	4.6
500	745	1701	3.629×10^{-6}	4.6

Table S14. Research status of TIMs

Fillers and substrates	Loading	K (W/m·K)	Degree of hot-spot cooling (°C)	Year and References
EG	20 wt%	0.60	-	2010 [4]
EG	30 wt%	1.20	-	2013 [5]
EG	0.5 wt%	1.31	-	2015 [6]
EG	1.81 wt%	10	-	2021 [7]
EG	24.89 wt%	19.6	-	2021 [8]
GN	1 wt%	1.42	-	2015 [9]
GN	1.5 wt%	2.7	2	2016 [10]
GN	3.0 wt%	0.49	-	2017 [11]
GN	9.5 wt %	2.13	-	2020 [12]
GN	7.2 wt %	0.51	-	2020 [13]
GO	7.0wt %	1.96	-	2020 [14]
GO	12.1 wt %	13.3	-	2021 [15]
GO	2.3 wt %	20	-	2021 [16]
CNT	1 wt%	0.285	-	2017 [17]
CNT	5.7wt%	0.516	-	2017 [18]
CNT	17 wt%	1.04	-	2018 [19]
CNT	1 wt%	1.36	-	2019 [20]
CNT	2 wt%	1.09	-	2019 [20]
CNT	0.5 wt%	0.70	-	2014 [21]
BN	50 wt%	1.74	-	2012 [22]
BN	15 vol%	6.07	-	2019 [23]
BN	50 wt%	13.2	-	2020 [24]
BN	40 wt %	5.86	-	2020 [25]
BN	60 wt%	7.62	-	2022 [26]
Si_3N_4	2 wt %	4.7	-	2020 [27]
Si_3N_4	0.85 wt %	1.3	-	2019 [28]
Si_3N_4	0.8 wt %	1.38	-	2016 [29]
Si_3N_4	1 wt%	3.8	-	2016 [29]
Si_3N_4	0.95 wt %	5.1	-	2016 [29]

Table S15. Research status of TIMs with thermal storage properties

Substrate	K(W/m·K)	Enthalpy of phase change (J/g)	Degree of hot-spot cooling (°C)	Year and References
EG	1.28	149.56	5.8	2022 [30]
EG	0.99	127.5	5.5	2021[31]
EG	0.25	199.2	-	2020 [32]
EG	2.50	163.5	-	2019 [33]
EG	0.51	128.1	-	2018 [34]
EG	7.20	115.2	-	2018 [35]
EG	10.37	96.8	-	2017 [36]
EG	3.60	145.0	-	2015 [37]
Graphene	5.11	133.6	-	2021 [38]
Graphene	3.2	153.1	14.3	2020 [39]
Graphene	3.11	169.3	-	2019 [40]
Graphene	0.41	167.8	-	2019 [41]
Graphene	1.03	182.6	-	2019 [42]
Graphene	1.46	154.1	-	2019 [43]
Graphene	0.92	161.0	-	2018 [44]
Graphene	0.62	200.0	-	2016 [45]
GO	0.35	176.7	-	2021 [46]
GO	0.48	158.2	-	2019 [47]
GO	1.72	157.7	-	2018 [48]
GO	1.89	143.6	-	2018 [48]
GO	1.84	145.9	-	2016 [49]
CNTs	2.8	142.1		2020 [50]
CNTs	3.49	59.9	-	2019 [51]
CNTs	2.40	119.4	-	2019 [52]
CNTs	1.023	155.7	-	2018 [53]
CNTs	7.27	121.1	-	2018 [54]
CNTs	1.83	166		2015 [55]
BN	0.31	189	-	2020 [56]
BN	0.261	191.6	-	2020 [57]
BN	0.32	191.7	-	2020 [58]
BN	0.084	205.4		2020 [59]
BN	0.28	162.1	-	2020 [60]
BN	0.3	158.3	-	2020 [61]
BN	0.45	55.76	-	2020 [62]
Si_3N_4	0.362	152.3	-	2016 [63]
Si_3N_4	0.32	133.47	-	2016 [64]
Si_3N_4	0.31	113.63	-	2014 [65]
HEPCF	**3.8**	**210**	**15/20**	**This work**

REFERENCES

[1] Z. Zhou, X. Zhou, Y. Peng, L. Li, J. Cao, L. Yang, B. Cao, *Applied Thermal Engineering* **2021**, 185, 116346.

[2] K. V. Sabarish, P. Paul, *Materials Today: Proceedings* **2020**, 22, 460.

[3] Y. Zhou, Y. Cui, X. Wang, M. Zhang, M. Zhang, Y. Gao, H. Wang, *Colloids and Surfaces A: Physicochemical and Engineering Aspects* **2021**, 628, 127361.

[4] Y. He, X.-s. Wu, Z.-c. Chen, presented at Advanced Polymer Processing International Forum, Qingdao, PEOPLES R CHINA, 2011

Oct 21-23, **2010**.

[5] Y. Yoo, H. L. Lee, S. M. Ha, B. K. Jeon, J. C. Won, S.-G. Lee, *Polymer International* **2014**, 63, 151.

[6] Y. Seki, Ş. İnce, M. A. Ezan, A. Turgut, A. Erek, *Solar Energy Materials and Solar Cells* **2015**, 140, 457.

[7] Y. Guo, K. Ruan, J. Gu, *Materials Today Physics* **2021**, 20, 100449.

[8] B. Wei, L. zhang, S. Yang, *Chemical Engineering Journal* **2021**, 404, 126437.

[9] Y. J. Noh, S. Y. Kim, *Polymer Testing* **2015**, 45, 132.

[10] H. Zhang, Y. Lin, D. Zhang, W. Wang, Y. Xing, J. Lin, H. Hong, C. Li, *Current Applied Physics* **2016**, 16, 1695.

[11] C. Silvestri, M. Riccio, R. H. Poelma, A. Jovic, B. Morana, S. Vollebregt, A. Irace, G. Q. Zhang, P. M. Sarro, *Small* **2018**, 14.

[12] C. Liang, M. Hamidinejad, L. Ma, Z. Wang, C. B. Park, *Carbon* **2020**, 156, 58.

[13] X. Yang, S. Fan, Y. Li, Y. Guo, Y. Li, K. Ruan, S. Zhang, J. Zhang, J. Kong, J. Gu, *Composites Part A: Applied Science and Manufacturing* **2020**, 128, 105670.

[14] C. Li, B. Zhang, B. Xie, X. Zhao, J. Chen, *Energy Conversion and Management* **2020**, 208, 112586.

[15] Y. Chen, X. Hou, M. Liao, W. Dai, Z. Wang, C. Yan, H. Li, C.-T. Lin, N. Jiang, J. Yu, *Chemical Engineering Journal* **2020**, 381, 122690.

[16] P. Liu, X. Li, P. Min, X. Chang, C. Shu, Y. Ding, Z.-Z. Yu, *Nano-Micro Letters* **2021**, 13.

[17] A. Karaipekli, A. Biçer, A. Sarı, V. V. Tyagi, *Energy Conversion and*

Management **2017**, 134, 373.

[18] X. Zhang, R. Wen, Z. Huang, C. Tang, Y. Huang, Y. Liu, M. Fang, X. Wu, X. Min, Y. Xu, *Energy and Buildings* **2017**, 149, 463.

[19] J. Han, G. Du, W. Gao, H. Bai, *Advanced Functional Materials* **2019**, 29.

[20] Y. Qu, S. Wang, D. Zhou, Y. Tian, *Renewable Energy* **2020**, 146, 2637.

[21] J.-M. Park, D.-J. Kwon, Z.-J. Wang, J.-U. Roh, W.-I. Lee, J.-K. Park, K. L. DeVries, *Composites Part B-Engineering* **2014**, 67, 22.

[22] S. Y. Pak, H. M. Kim, S. Y. Kim, J. R. Youn, *Carbon* **2012**, 50, 4830.

[23] J. Chen, X. Huang, B. Sun, P. Jiang, *Acs Nano* **2019**, 13, 337.

[24] Z.-G. Wang, W. Liu, Y.-H. Liu, Y. Ren, Y.-P. Li, L. Zhou, J.-Z. Xu, J. Lei, Z.-M. Li, *Composites Part B-Engineering* **2020**, 180.

[25] Z. Liu, J. Li, X. Liu, *Acs Applied Materials & Interfaces* **2020**, 12, 6503.

[26] Q. Hu, X. Bai, C. Zhang, X. Zeng, Z. Huang, J. Li, J. Li, Y. Zhang, *Composites Part A-Applied Science and Manufacturing* **2022**, 152.

[27] A. Shimamura, Y. Hotta, H. Hyuga, M. Hotta, K. Hirao, *Scientific Reports* **2020**, 10, 14926.

[28] Y. Yuan, Z. Li, L. Cao, B. Tang, S. Zhang, *Ceramics International* **2019**, 45, 16569.

[29] A. Shimamura, Y. Hotta, H. Hyuga, N. Kondo, K. Hirao, *Journal of the Ceramic Society of Japan* **2015**, 123, 908.

[30] D.-L. Han, L.-Y. Yang, S.-P. Wang, X.-Q. Zeng, L. Tang, K. Liu, K. Liang, H.-Q. Shen-Tu, L.-Q. Guo, L. Bai, Y.-C. Huang, *Journal of Materials Science: Materials in Electronics* **2022**, 33, 1008.

[31] L.-Y. Yang, C.-P. Feng, L. Bai, R.-Y. Bao, Z.-Y. Liu, M.-B. Yang, W. Yang, *Chemical Engineering Journal* **2021**, 425, 131466.

[32] C. Li, B. Zhang, Q. Liu, *Journal of Energy Storage* **2020**, 29, 101339.

[33] C. Li, B. Zhang, B. Xie, X. Zhao, J. Chen, Z. Chen, Y. Long, *Sustainable Cities and Society* **2019**, 44, 458.

[34] Y. Lin, C. Zhu, G. Alva, G. Fang, *Applied Energy* **2018**, 228, 1801.

[35] T. Wang, Y. Jiang, J. Huang, S. Wang, *Applied Energy* **2018**, 218, 184.

[36] T. Wang, S. Wang, W. Wu, *International Journal of Heat and Mass Transfer* **2017**, 109, 930.

[37] H. Tabassum, X. Huang, R. Chen, R. Zou, *Journal of Materiomics* **2015**, 1, 229.

[38] F. Wei, C.-P. Feng, J. Yang, L.-Y. Yang, L. Bai, R.-Y. Bao, Z.-Y. Liu, M.-B. Yang, W. Yang, *ACS Applied Materials & Interfaces* **2021**, 13, 59364.

[39] W. Li, F. Wang, W. Cheng, X. Chen, Q. Zhao, *Energy Conversion and Management* **2020**, 210, 112680.

[40] T. Qian, S. Zhu, H. Wang, A. Li, B. Fan, *ACS Sustainable Chemistry & Engineering* **2019**, 7, 2446.

[41] Y. Zhang, J. Wang, J. Qiu, X. Jin, M. M. Umair, R. Lu, S. Zhang, B. Tang, *Applied Energy* **2019**, 237, 83.

[42] X. Wei, F. Xue, X.-d. Qi, J.-h. Yang, Z.-w. Zhou, Y.-p. Yuan, Y. Wang, *Applied Energy* **2019**, 236, 70.

[43] F. Xue, Y. Lu, X.-d. Qi, J.-h. Yang, Y. Wang, *Chemical Engineering Journal* **2019**, 365, 20.

[44] J. Yang, G.-Q. Qi, R.-Y. Bao, K. Yi, M. Li, L. Peng, Z. Cai, M.-B. Yang, D. Wei, W. Yang, *Energy Storage Materials* **2018**, 13, 88.

[45] L. Zhang, R. Li, B. Tang, P. Wang, *Nanoscale* **2016**, 8, 14600.

[46] S. Xi, M. Wang, L. Wang, H. Xie, W. Yu, *Solar Energy Materials and Solar Cells* **2021**, 226.

[47] Y. Xia, H. Zhang, P. Huang, C. Huang, F. Xu, Y. Zou, H. Chu, E. Yan, L. Sun, *Chemical Engineering Journal* **2019**, 362, 909.

[48] J. Yang, L.-S. Tang, L. Bai, R.-Y. Bao, Z. Liu, B.-H. Xie, M.-B. Yang, W. Yang, *ACS Sustainable Chemistry & Engineering* **2018**, 6, 6761.

[49] J. Yang, L.-S. Tang, R.-Y. Bao, L. Bai, Z.-Y. Liu, W. Yang, B.-H. Xie, M.-B. Yang, *Journal of Materials Chemistry A* **2016**, 4, 18841.

[50] A. Li, C. Dong, W. Dong, F. Yuan, H. Gao, X. Chen, X.-B. Chen, G. Wang, *Advanced Electronic Materials* **2020**, 6, 1901428.

[51] W. Zhu, N. Hu, Q. Wei, L. Zhang, H. Li, J. Luo, C.-T. Lin, L. Ma, K. Zhou, Z. Yu, *Materials & Design* **2019**, 172, 107709.

[52] W. Aftab, A. Mahmood, W. Guo, M. Yousaf, H. Tabassum, X. Huang, Z. Liang, A. Cao, R. Zou, *Energy Storage Materials* **2019**, 20, 401.

[53] A. Li, J. Wang, C. Dong, W. Dong, D. G. Atinafu, X. Chen, H. Gao, G. Wang, *Applied Energy* **2018**, 217, 369.

[54] Q. Zhang, J. Liu, *Solar Energy Materials and Solar Cells* **2018**, 179, 217.

[55] I. Kholmanov, J. Kim, E. Ou, R. S. Ruoff, L. Shi, *ACS Nano* **2015**, 9, 11699.

[56] X. Jia, Q. Li, C. Ao, R. Hu, T. Xia, Z. Xue, Q. Wang, X. Deng, W. Zhang, C. Lu, *Composites Part A: Applied Science and Manufacturing* **2020**, 129, 105710.

[57] B. Xie, C. Li, J. Chen, N. Wang, *Solar Energy* **2020**, 204, 624.

[58] G. Yang, L. Zhao, C. Shen, Z. Mao, H. Xu, X. Feng, B. Wang, X. Sui, *Solar Energy Materials and Solar Cells* **2020**, 209, 110441.

[59] Y. Xia, W. Cui, R. Ji, C. Huang, Y. Huang, H. Zhang, F. Xu, P. Huang, B. Li, L. Sun, *Colloids and Surfaces A: Physicochemical and Engineering Aspects* **2020**, 586, 124225.

[60] J. Huang, B. Zhang, M. He, X. Huang, G. Wu, G. Yin, Y. Cui, *Journal of Materials Science* **2020**, 55, 7337.

[61] P. Yan, F. Luo, B. Huang, L. Xiao, Q. Qian, H. Li, Q. Chen, *Chinese Journal of Applied Chemistry* **2020**, 37, 46.

[62] H. Wang, J. Lei, T. Wu, D. Wu, H. Liu, Y. Deng, F. Wu, *ACS Omega* **2022**, 7, 2438.

[63] X. Zhang, H. Liu, Z. Huang, Z. Yin, R. Wen, X. Min, Y. Huang, Y. Liu, M. Fang, X. Wu, *Chemical Engineering Journal* **2016**, 301, 229.

[64] N. Sun, Z. Xiao, *Journal of Materials Science* **2016**, 51, 8550.

[65] Y. Yang, J. Luo, G. Song, Y. Liu, G. Tang, *Thermochimica Acta* **2014**, 597, 101.